PNAS RESEARCH ARTICLE | BIOPHYSICS AND COMPUTATIONAL BIOLOGY

Conformational free energy landscape of a glutamate transporter and microscopic details of its transport mechanism

Sundar Thangapandian[a,b,c], Ashkan Fakharzadeh[a,b,c], Mahmoud Moradi[d], and Emad Tajkhorshid[a,b,c,e,1]

Affiliations are included on p. 9.

Edited by Olga Boudker, Weill Cornell Medicine, New York, NY; received August 14, 2024; accepted January 21, 2025

Removing glutamate from the synaptic cleft is vital for proper function of the brain. Excitatory amino acid transporters mediate this process by uptaking the neurotransmitter from the synaptic cleft back to the cell after its release. The archaeal homolog, Glt_{Ph}, an aspartate transporter from *Pyrococcus horikoshii*, presents the best structurally characterized model for this family of transporters. In order to transport, Glt_{Ph} undergoes elevator-like conformational changes between inward-facing (IF) and outward-facing (OF) states. Here, we characterize, at an atomic level, the OF⇌IF transition of Glt_{Ph} in different *apo*/bound states using a combination of ensemble-based enhanced sampling techniques, employing more than two thousand of coupled simulation replicas of membrane-embedded Glt_{Ph}. The resulting free-energy profiles portray the transition of *apo*/bound states as a complex four-stage process, while sodium binding alone locks the structure in one of its states. Along the transition, the transport domain (TD) disengages from the scaffold domain (SD), allowing it to move as a piston sliding vertically with respect to the membrane during the elevator-like motion of TD. Lipid interactions with residues comprising the SD–TD interface directly influence the large-scale conformational changes and, consequently, the energetics of transport. Structural intermediates formed during the transition leak water molecules and may correlate to the uncoupled Cl^- ion conductance observed experimentally in both prokaryotic and mammalian glutamate transporters. Mechanistic insights obtained from our study provide a structural framework for better development of therapeutic for neurological disorders.

membrane transporter | molecular dynamics | enhanced sampling | free energy

Significance

The synaptic concentration of glutamate, a key excitatory neurotransmitter in the brain, is regulated by transporters that undergo large-scale transitions via the elevator transport mechanism. Despite significant efforts, the details of these transitions remain elusive. This study elucidates the conformational transition of the glutamate transporter Glt_{Ph}, a model for excitatory amino acid transporters, using advanced ensemble-based enhanced sampling techniques. Our findings uncover a complex four-stage transition process, emphasizing the roles of ions and lipid interactions in transporter energetics, and highlight that the transition does not occur with partial binding. This detailed atomic-level insight advances our understanding of neurotransmitter regulation and provides a structural blueprint to guide therapeutic interventions for neurological disorders linked to the transporter dysfunction.

Mammalian excitatory amino acid transporters (EAATs) play a crucial role in rapid clearance of synaptic glutamate, the most important excitatory neurotransmitter in the central nervous system (1–4). Dysregulation of EAATs has been associated with a spectrum of neurological conditions such as depression, schizophrenia, stroke, Parkinson's, and Alzheimer's diseases (5–8). Consequently, they hold promise as a therapeutic target for modulating glutamate concentration in the synapse and addressing associated disorders.

The glutamate transporters are members of the solute carrier 1 (SLC1) family of secondary active transporters, where the transport mechanism is driven by the electrochemical gradient of cotransported ions, particularly Na^+, facilitating the uphill transport of glutamate and/or aspartate (9–14). They also exhibit thermodynamically uncoupled Cl^- conductance, resulting in an overall uncoupled, but glutamate-gated anion channel activity (15–18), where the conducting state is likely a transient intermediate of the elevator-like transition (18–22). Eukaryotic glutamate transporters move one glutamate into the cell along with three Na^+ ions and one H^+, while releasing one K^+ ion (23–25) in each transport cycle. In contrast, archaeal counterparts preferentially transport aspartate over glutamate, and their function is independent of proton or potassium (26, 27). The crystal structures of archaeal glutamate transporter homolog Glt_{Ph} from *Pyrococcus horikoshii* have provided crucial insights, offering direct structural evidence for the mechanism of substrate translocation through elevator-type conformational changes (4, 12, 18, 28–37). With over 30% sequence identity to EAATs, Glt_{Ph} serves as an excellent structural model for studying the elevator-like mechanism in this family.

Glt_{Ph} is a homotrimer with each protomer composed of two distinct domains, a relatively static scaffold domain (SD) and a highly dynamic transport domain (TD) containing the substrate/ion binding sites (29, 32, 38–40), as illustrated in Fig. 1 *A*–*C*. Each protomer contains eight transmembrane α-helices (TM1-8) and two helical

Author contributions: S.T., M.M., and E.T. designed the research; S.T., A.F., and M.M. performed the simulations and analyzed the data; E.T. funding, resources; and S.T., A.F., M.M., and E.T. wrote the paper.

The authors declare no competing interest.

This article is a PNAS Direct Submission.

[1]To whom correspondence may be addressed. Email: emad@illinois.edu.

This article contains supporting information online at https://www.pnas.org/lookup/suppl/doi:10.1073/pnas.2416381122/-/DCSupplemental.

Published March 5, 2025.

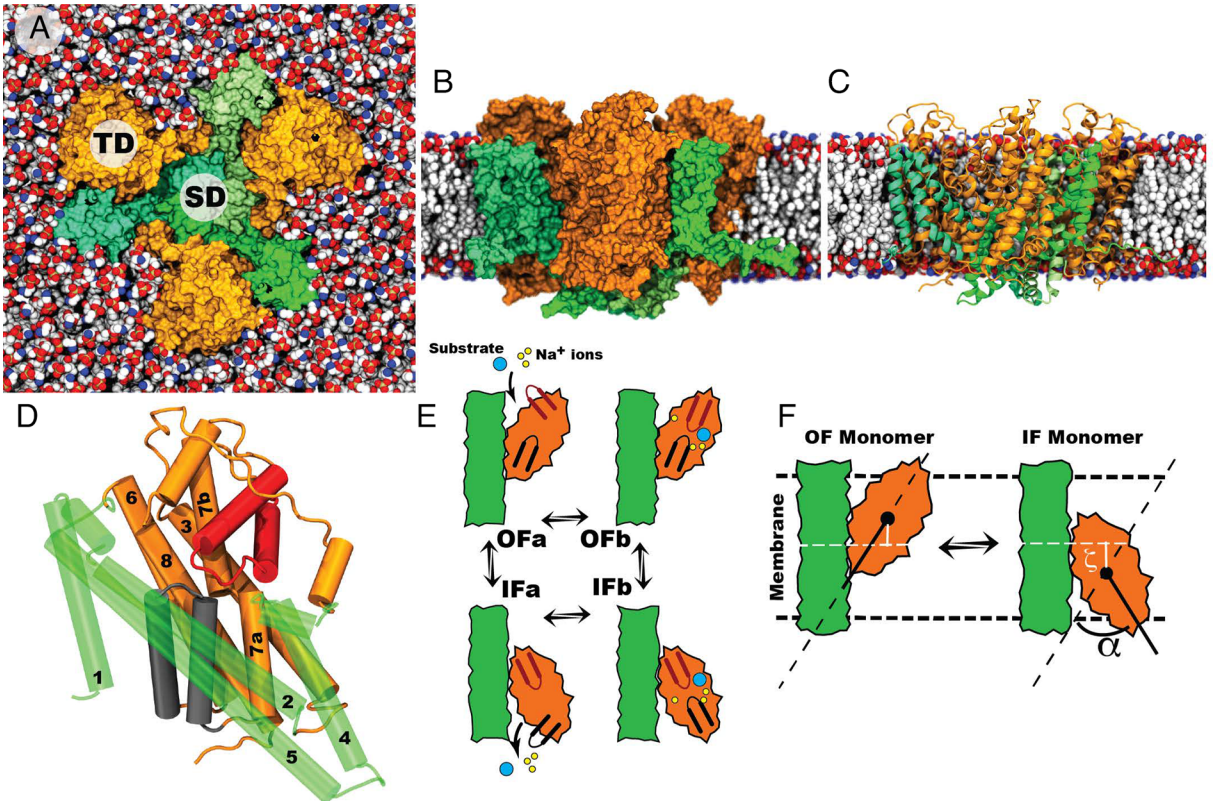

Fig. 1. Structural details and transport cycle of Glt_{Ph}. Trimeric Glt_{Ph}, in OF state, embedded in a POPE lipid bilayer. Scaffold domains (SDs) and transport domains (TDs) are colored in shades of green and orange, respectively. SDs form the trimeric core, to which TDs are attached [(*A*) *Top* view; (*B* and *C*) side views of the system with front lipid molecules hidden for clarity. (*B*) shows the protein in surface and (*C*) in cartoon representation]. (*D*) Cartoon representation of a Glt_{Ph} protomer highlighting the eight TM helices and the two helical hairpins (HP1 in gray and HP2 in red). (*E*) Schematic of the transport cycle and (*F*) the collective variables (CVs) used to drive the OF ⇌IF transition and used to describe its free-energy landscape. α and ζ represent the rotation and translation of TD with respect to SD, respectively.

hairpins (HP1 and HP2), as depicted in Fig. 1 *D* and *E*. The protomers are expected to move and transport substrate independently (32, 41–47).

Glt_{Ph} exhibits an elevator-like conformational transition during its transport cycle. In order to ensure tight coupling of cotransported species, this transition is only allowed energetically when the transporter is either in an *apo* state or in its fully bound, i.e., in complex with both the substrate and all three sodium ions. During the transport, the SD remains relatively steady, but the TD undergoes substantial rotational and translational movements in the membrane, transitioning the protein between the inward-facing (IF) and outward-facing (OF) states. The transition switches the accessibility of the substrate/ion binding sites between the cytoplasmic and extracellular sides of the membrane (4, 28, 29, 32, 39, 43, 44, 48). Various crystallographic, computational, and biochemical studies have characterized the three sites for Na^+ ions in Glt_{Ph} that are cotransported along with the substrate (29, 49–51). The alternating-access mechanism is believed to be accompanied by the opening and closing of HP1 and HP2 controlling the accessibility of the binding sites to the surrounding solution (4, 29, 52–59). Comparative analysis of OF and IF crystal structures reveals an 18-Å translation and a 37° rotation of the TD between the two states. Despite extensive structural and biochemical investigations of Glt_{Ph} and EAATs, the atomic-level details of their large-scale structural transitions and the nature of intermediates remain unknown.

Here, using comprehensive ensemble-based, enhanced sampling simulations, and free-energy calculations employing system-specific reaction coordinates, we present a complete energetic description of the Glt_{Ph} OF⇌IF transition in its fully bound (Glt_{fb}), *apo* (Glt_{apo}), and partially bound (Glt_{pb}) states. Our approach involves stepwise integration of various simulation techniques over a cumulative simulation time exceeding 100 μs.

The bias-exchange umbrella sampling (BEUS) (60–62), in 2 dimensions (2D), serves here as the primary sampling tool. The method is used to examine the conformational free-energy landscape of Glt_{Ph} using meticulously chosen, specific reaction coordinates or CVs to best represent the underlying physics. Given the complexity of the energy landscapes, iterative sampling was imperative to optimize the reaction coordinates, and sample more relevant regions of the configuration space (61, 62). String method (63–65) and other path-finding algorithms (66, 67) are then employed to refine the initial minimum-energy paths in high-dimensional spaces, which are used in the subsequent 1D BEUS simulations.

Employing this refined pathway and our approach, we describe energetically the OF⇌IF conformational transition pathway of Glt_{Ph} under different binding conditions, thereby providing an atomic-detailed framework for the chemomechanical coupling in the system. Our findings offer a detailed perspective on the large-scale conformational changes in Glt_{Ph}, revealing a complex, four-stage transition marked by a highly coupled two-component transition of TD, unveiling comparable yet distinguishable structural transition pathways for Glt_{fb} and Glt_{apo}. The disparity between the energetics of Glt_{fb} and Glt_{apo} conformational transition pathways underscores the involvement of multiple intermediates in the mechanism. Furthermore, some of the occluded intermediates obtained from our simulations exhibit

water conduction and thus may substantiate the uncoupled Cl^- conduction. On the other hand, our simulations consistently indicate that Glt_{pb} remains locked in its OF state throughout. These observations align with the alternating-access and elevator-like mechanisms, emphasizing the specific role played by ions and the helical hairpin gate in controlling the transition. The resulting similar but somewhat different free-energy profiles for different protomers hint at the effect of lipids on the energetics of transport.

1. Results and Discussion

1.1. Pathway and Energetics of Glt_{Ph} Conformational Transition. The calculated 2-dimensional free-energy landscape of Glt_{fb} describes its OF⇌IF transition approximately as a 4-stage process (Fig. 2*A*). Starting from the OF state (*Right* side of the diagram), the first stage consists of a brief translation (∼2 Å) of TD toward its position in the IF state. Stage 2 involves a combination of TD translation and rotation (∼2 Å and ∼5°, respectively). Stage 3 is best described as a long TD translation-only phase (∼6 Å), while the final stage (Stage 4) is a predominantly TD rotation stage (∼30°) combined with a smaller translation component (∼5 Å). The energy landscape shows multiple minima along the OF⇌IF transition of Glt_{fb}. It is worth noting the IF region in our free-energy map deviates from the experimental IF rotation and translation values, as indicated by the black boxes in our free-energy maps. The experimental IF values were derived from directly from the crystallized structure [PDB ID: 3KBC (29)], which was obtained under specific experimental conditions. A broad energy minimum at the *Top Left* (IF space) of the landscape (Fig. 2*A*) represents the heterogeneity of the IF conformational ensembles of the three protomers sampled during the simulations. We speculate that the differences in interaction patterns with lipids are a major source for this heterogeneity. The free-energy profiles for individual protomers are provided in *SI Appendix, Supplementary Note* 1 and Fig. S1.

During the transition, Glt_{fb} crosses two significant free-energy barriers (3.9 and 4.3 kcal/mol, respectively) while transitioning through Stages 2 and 3 (Fig. 2*A*), as well as a lower barrier when going through Stage 4 (2.6 kcal/mol). It visits a stable intermediate between Stages 3 and 4 with a free energy of only ∼1 kcal/mol higher then the IF and OF end states, which, interestingly, exhibit similar free energies (Fig. 2*A*). Representative conformations corresponding to this intermediate and to the OF and IF minima derived from the simulations are shown in Fig. 3. The PDB files of these conformations (OF.pdb, IN.pdb, and IF.pdb) have been provided in *SI Appendix*.

The energy landscape of Glt_{apo} has a similar overall shape but exhibits slightly different barriers (Fig. 2*B*). The first barrier (3.8 kcal/mol) is encountered after Stage 1 and is located almost exactly at the same place as in Glt_{fb}. The second and broader barrier is about 6.0 kcal/mol, i.e., about 1.7 kcal/mol higher than the corresponding value in Glt_{fb}. This barrier happens between Stages 3 and 4 where the transition includes a large TD orientational component (Fig. 2 *B* and *D*). Notably, the free-energy profiles for both the Glt_{fb} and Glt_{apo} states are characterized by energy barriers of ≤6 kcal/mol. This barrier is generally consistent with the symport mechanism of the transporter, where such transitions are feasible at room temperature, aligning with biologically feasible reaction rates for physiological transport processes.

IF conformations of the three Glt_{apo} protomers converged to a more confined region of the configuration space when compared to Glt_{fb} and showed ∼2 Å less TD translations. This suggests that Glt_{Ph} in its fully bound conformations might move farther toward the intracellular side than in the *apo* conformation. The additional translation in Glt_{fb} could facilitate the unloading of

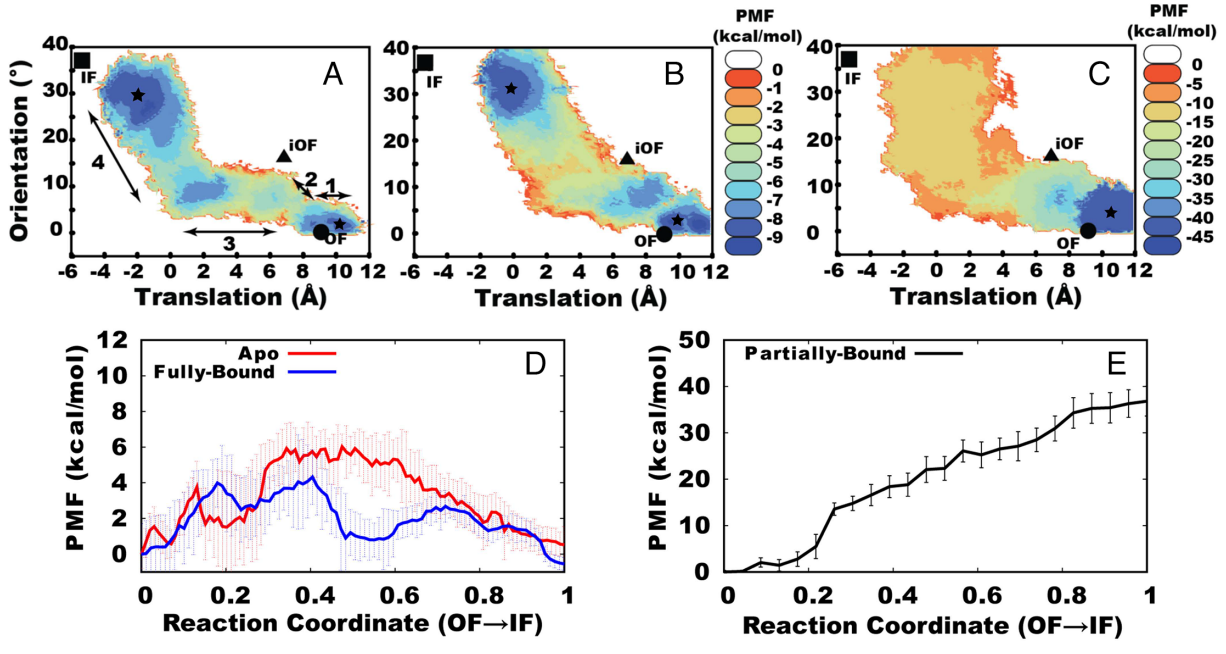

Fig. 2. Free-energy maps of Glt_{Ph} OF⇌IF transitions in different bound states. Potential of mean force (PMF) profiles of OF⇌IF transitions in (*A*) Glt_{fb}, (*B*) Glt_{apo}, and (*C*) Glt_{pb} shown in a 2D space. Note the different energy scale in (*C*). 1D PMF profiles of Glt_{fb} and Glt_{apo} (*D*) and Glt_{pb} (*E*). The Glt_{pb} system shows no free-energy minima in the IF conformation (*C* and *E*), reflecting that it essentially remains locked in the starting OF conformation. The numbered arrows in (*A*) indicate how the Glt_{fb} OF⇌IF transition can be approximately divided into 4 stages (see text for details). The circle, square, triangle, and star in (*A*–*C*) represent the positions of OF [PDB 2NWX (4)], IF [PDB 3KBC (29)], iOF [PDB 3V8G (30)] Glt_{Ph} crystal structures, and the main minima, respectively [see Fig. 3 for representative structures of minima in (*A*), indicated by star]. The error bars represent the SD based on 32 copies for each image (*SI Appendix, Methods*).

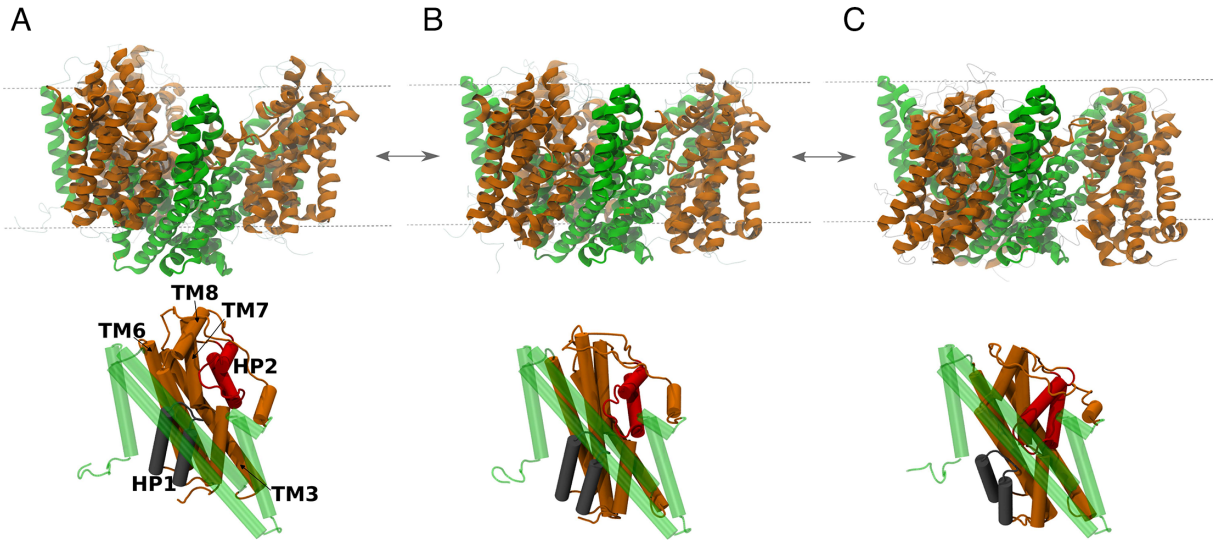

Fig. 3. Glt_{fb} snapshots corresponding to the minima observed in the free-energy landscape shown in Fig. 2*A*. The sample conformations of (*A*) OF, (*B*) intermediate, and (*C*) IF states are presented in both trimeric (*Top*) and monomeric (*Bottom*) side views. The intermediate state visited at the end of the Stage 3 exhibits a free energy of approximately 1 kcal/mol higher than the IF and OF end states. SDs and TDs are colored in green and orange, respectively. Helical hairpins, HP1 and HP2, which are key to the mechanism, are colored in gray and red in the *Bottom* figures. The approximate position of the membrane is shown with horizontal lines highlighting the displacements of both TD and SD relative to the membrane during the transport cycle.

the bound substrate and Na^+ ions. The stable intermediate observed in the middle of the transition in Glt_{fb} system does not show in Glt_{apo}, but an equally stable state is observed much earlier in the transition and close to the crystallographically solved intermediate OF (iOF) state (30) [PDB ID. 3V8Gc (30)]. The occurrence of stable intermediate conformations at different regions of the configuration space in Glt_{fb} and Glt_{apo} hints at different conformational pathways despite comparable free-energy profiles.

In the partially bound case of Glt_{pb}, the transition is accompanied with a substantial rise in the free energy, and no minimum can be even gained in the region corresponding to the IF state (Fig. 2 *C* and *E*). All three protomers show this behavior independently (*SI Appendix*, Fig. S1). In other words, the transporter remains locked in the OF state, the state from which we initiated our sampling, when only a single Na^+ ion is bound to it. However, it is possible that an IF state exists in the presence of Na^+ that our sampling strategy has not been able to capture. For instance, a Na^+-bound IF structure of Glt_{Ph}, PDB ID. 6X13, has been recently crystallized (34). Although the mechanistic details of the differences between the partially bound and other cases (fully bound or apo) require further detailed examination of the simulations, they are consistent with and can be attributed to the restriction that global flipping of the transporter should be prohibited in the partially bound configuration. This selective transition is a fundamental aspect of the transporter's role in synaptic neurotransmitter regulation and it may arise as the partially bound state lacks the necessary coordination of ions and substrate to stabilize the transporter in conformations that facilitate a complete transition. Moreover, such a condition could dissipate the physiological concentration gradients of Na^+ and glutamate, thereby unfavorably affecting the membrane potential.

1.2. Disengagement of the Transport Domain. The interface between the SD and TD is mostly hydrophobic, except for a small polar region formed by the tip of HP1 (*SI Appendix*, Fig. S3). During the large-scale OF⇌IF transition of the protein, the SD/TD interfacial area is reduced by about 200 to 300 $Å^2$ in the intermediate states as compared to the OF and IF end states (*SI Appendix*, *Supplementary Note 2* and Fig. 4 *A* and *B*). The OF and IF end states show SD/TD interfacial areas of 1,770 and 1,682 $Å^2$, respectively, whereas the area corresponding to the intermediate states is reduced to 1,440 and 1,515 $Å^2$ (Fig. 4*B*). We hypothesize that sliding of the hydrophilic tip of HP1 (*SI Appendix*, Fig. S3*B*) over the hydrophobic surface of SD may have induced the observed disengagement of the TD during the initial part of the transition. In the later part of the transition, the interfacial area increases back as the highly hydrophobic HP2 meets the SD and establishes favorable interactions before reaching the IF state. Reduced interfacial contact area in the intermediate states correlates well with the increased water in this region (*SI Appendix*, Fig. S2*A*). Similar conclusions about the disengagement of the two domains during the transport cycle have been reported in mutagenesis studies of Glt_{Ph} by Akyuz et al. (68), where the rate of substrate transport was increased by engineering mutations at the interface that facilitated their separation, thereby enhancing the dynamic behavior of the transport domains.

1.3. Displacement of Both Scaffold Domain and Transport Domain in Membrane. The bowl-like central core of trimeric Glt_{Ph} formed by the three SDs functions as a rigid base to which the three TD domains are attached. While the TD domains undergo large-scale conformational transitions independent of each other, SD dynamics have been reported to be limited (43). However, both the SDs and TDs are in contact with the membrane and the movement of the TDs relative to the SDs is expected to be accompanied by the adjustment of both within the membrane (Fig. 3 *A*–*C*). In our extensive simulations, the SDs move like a piston during the OF⇌IF transition by ∼8 Å with respect to the membrane (Movies S1–S3). During Stages 1-3, SDs and TDs move in the opposite directions, while in Stage 4, they move in the same direction to complete the transition (Fig. 4 *C* and *D*). This interesting characteristic is facilitated by the reunion of the disengaged TDs with the SDs

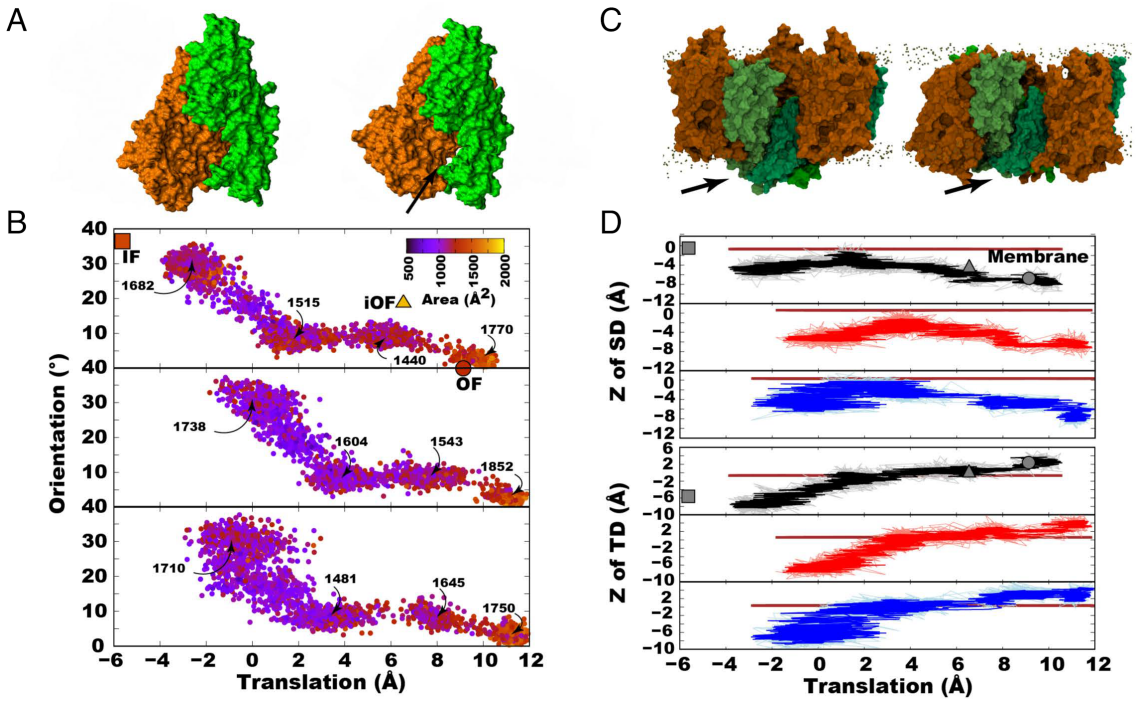

Fig. 4. Key structural changes during the OF⇌IF transition in Glt_{Ph}. (*A*) Two snapshots showing the disengagement of TD from SD. The snapshots correspond to protomer A in the OF state and an intermediate state where SD and TD are separated. A black arrow points to the region of separation. (*B*) Interfacial contact surface area between SD and TD for protomer A supporting their separation during the transition. *Top*, *Middle*, and *Bottom* plots represent Glt_{fb}, Glt_{apo}, and Glt_{pb} systems, respectively. Contact numbers calculated between SD and TD also support this behavior (Extended Data *SI Appendix*, Fig. S6*D*). (*C*) Structural snapshots highlighting two different locations of SD relative to the membrane representing the observed piston-like movement of SD during the transition (Movies S1–S3). Black arrows point to the movement of SD. (*D*) Centers of masses (CoMs) of SD (*Top*) and TD (*Bottom*) with respect to the membrane midplane (brown line) during the OF⇌IF transition. The solid lines correspond to a moving average done over a window size of 10. Black, red, and blue traces represent Glt_{fb}, Glt_{apo}, and Glt_{pb} systems, respectively. Circle, square, and triangle indicators represent the corresponding values for the OF, IF, and iOF crystal structures, respectively. The position of the membrane in the case of crystal structures was obtained from their individual 200-ns simulations (*SI Appendix*, *Supplementary Note* 8).

and indicates that SD–TD interactions are key in stabilizing the end states. The center of mass (CoM) of SD in the OF state is located ∼8 Å below the midplane of the membrane. As the OF⇌IF transition progresses, it moves upward almost to the membrane midplane, and upon the completion of the transition, it returns to ∼6 Å below the membrane midplane (Fig. 4 *C* and *D*). Interestingly, most of the rotation/translation occurs while SD moves away/toward the membrane midplane (*SI Appendix*, Fig. S4). Movement of SD and TD with respect to membrane are discussed in *SI Appendix* in more detail (*SI Appendix*, *Supplementary Note* 3 and Fig. S4). In contrast, the translation of the TD along the membrane normal is rather monotonic, with its CoM moving from ∼4 Å above the membrane midplane in the OF state to ∼8 Å below it in the IF state.

1.4. Local Conformational Changes. Local conformational changes underlie the large-scale, global motions in biomolecules. In case of Glt_{Ph}, some of these local changes are noteworthy. A salt bridge (SB) between E192 on TM5 and K290 on HP1 is a key stabilizing interaction of the OF state. This SB needs to break during the translation of TD toward its IF position. All systems show strong interactions between these SB-forming residues around the OF conformations throughout our extensive simulations (Fig. 5 *A* and *C*, and *SI Appendix*, Fig. S5). Glt_{fb} maintained a stronger SB interaction than Glt_{apo} and Glt_{pb} indicating the higher stability of TD when Glt is fully bound. The high free-energy barrier observed in the *Middle* of Stage 3 correlates well with the breaking of this SB (Figs. 2*A* and 5*C*).

TM7, the broken central helix of TD, is another structural element that undergoes a notable local conformational change during the OF⇌IF transition. The N-terminal part of TM7 (referred to as TM7a) faces the intracellular side, while the C-terminal part (TM7b) faces the extracellular side (Fig. 5*B*). Average tilt angle of TM7a in protomer A of Glt_{fb} initially drops from 8.1° in the OF state to 3.8° in the middle but later rises to 9.9° in the IF state. Average change in the tilt angle of TM7a helix in protomers A and B of Glt_{fb} is ∼4-6° smaller than those in Glt_{apo} and Glt_{pb}, probably due to incomplete occupation of the binding sites which allows additional flexibility of TM7a (Fig. 5*D* and *SI Appendix*, Fig. S5 *D* and *F*). The middle of TM7 forms part of the substrate and ion binding sites, and thus binding of small molecules at this site can directly couple to the structural dynamics of the helix. The tilt angles of TM7a in protomer A are 11.1°, 15.0°, and 17.2° in the OF, iOF, and IF crystal structures, respectively. The membrane environment present in the simulations may have significantly contributed to the difference compared to X-ray structures. Further details on local conformational changes are discussed in *SI Appendix*, *Supplementary Note* 4. Binding site conformational dynamics are also further discussed in *SI Appendix*, *Supplementary Note* 5.

1.5. Alternating Access Mechanism. Similar to other active, coupled transporters, Glt_{Ph} follows the general alternating access mechanism in which the substrate cannot be accessible from both sides of the membrane at any given time (69). During the transition between the OF and IF states, however, the substrate can become temporarily inaccessible from both sides

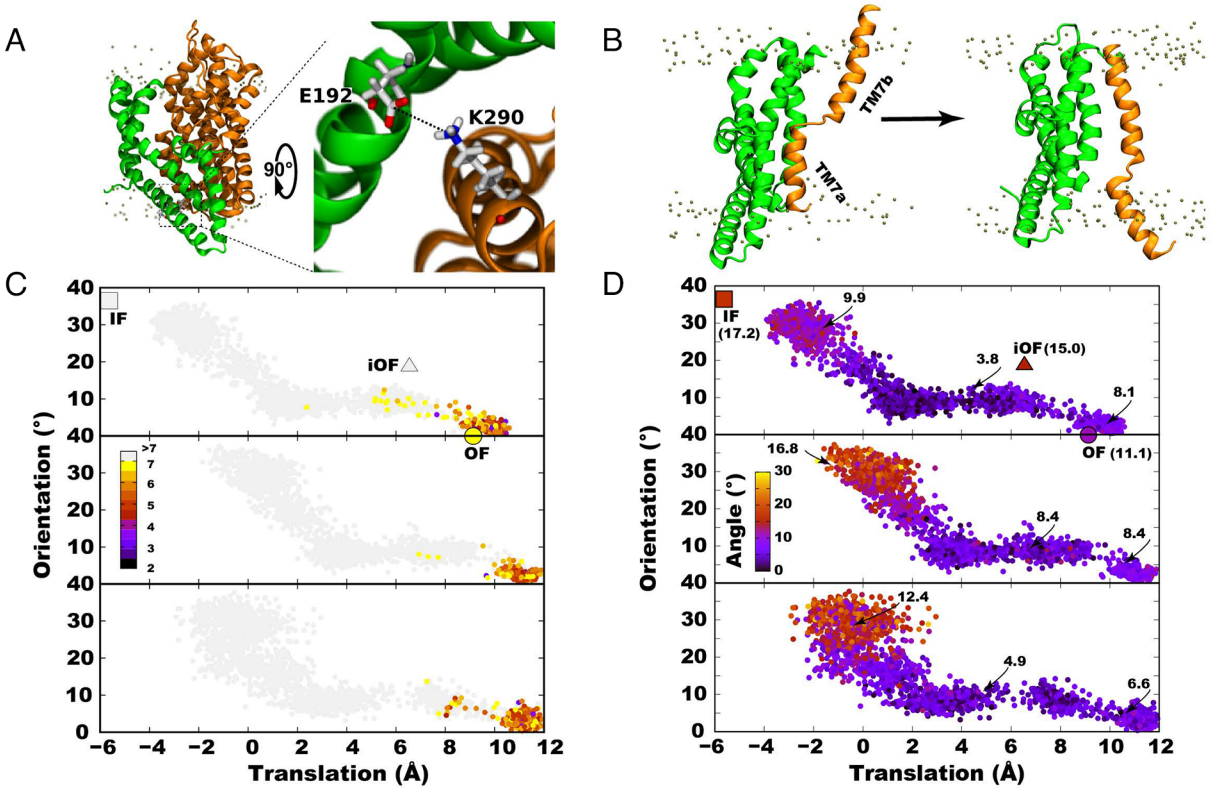

Fig. 5. Local conformational changes during the OF⇌IF transition of Glt_{Ph}. (*A*) Salt bridge (SB) between K290 in TM5 and E192 in HP1, and (*C*) its distance during the transition. The distance is measured as the distance between atom NZ in K290 and the mass center of atoms CD, OE1, and OE2 in E192. (*B*) Cartoon representation of TM7 in OF and IF conformations. TM7 is a broken TM helix located in the middle of TD and taking part in substrate binding site. For clarity, only TM7 (orange) from the TD is shown along with full SD (green). Phosphorus atoms of the membrane lipids are shown as brown beads. (*D*) Tilt angle of TM7a (intracellular half of TM7) with respect to the membrane in protomer A during the transition. Average values of different regions are indicated on the plot for easier comparison. In (*C* and *D*), *Top*, *Middle*, and *Bottom* plots represent Glt_{fb}, Glt_{apo}, and Glt_{pb}, respectively. Circle, square, and triangle indicators represent OF, IF, and iOF crystal structures, respectively.

of the membrane, before the transporter reaches the IF state and releases its cargo to the intracellular side of the membrane. Such "occluded" conformations have been found to be leaky to smaller molecules, e.g., water (70), and can be connected to the experimentally observed uncoupled Cl^- conductance in this family of transporters (3, 18, 22, 71, 72). In order to quantify the movements of the HP helices, which are crucial structural elements in substrate binding and accessibility, Cα-Cα distances of two residue pairs were calculated: i) between V198 in TM5 of SD and V355 at the tip of HP2; and, ii) between V51 in TM2 of SD and S277 at the tip of HP1. These distances quantify the extracellular (EC) and intracellular (IC) lock distances, respectively. Furthermore, the HP tip–tip distance (HP1–HP2 distance) was monitored as a metric for the stability of the binding site. The HP tip–tip distance remains small during the transition in Glt_{fb} (Fig. 6*B* and *SI Appendix*, Fig. S6*A*). Larger HP tip–tip distances are observed during the OF⇌IF transition of Glt_{apo}, suggesting that substrate/Na^+ binding structurally stabilizes the HPs in Glt_{fb}. Detailed definitions of the HP tip–tip distance and EC/IC lock distances are provided in *SI Appendix*, *Supplementary Note 6*. Glt_{fb} occluded conformations displayed a lower number of water molecules around the HP tips compared to other systems in accord to a more stable binding site in Glt_{fb} (Fig. 6*C* and *SI Appendix*, Fig. S6*B*).

During the transition, the EC lock displayed a ∼15 Å closure (Fig. 6*D*), while the IC lock showed a ∼10 Å opening (Fig. 6*E*), in complete accord with the alternating-access mechanism. Glt_{fb} displays a clearer EC closing and IC opening during the transition toward the IF state, while Glt_{apo} and Glt_{pb} are associated with more fluctuating EC/IC locks due to their higher dynamic, unbound HPs.

The simulated OF⇌IF transitions sample the crystallographically observed EC/IC distances for all OF, IF, and iOF states (Fig. 6 *D* and *E* and *SI Appendix*, Fig. S7 *A–D*). The translation of TD is a major component in EC closing during the early stages of the transition, while in later stages, its rotation contributes substantially to IC opening. The 2D space of EC and IC lock dynamics shows that Glt_{fb} transitions via one path, where both EC and IC locks alternated in a coordinated manner (Fig. 6*F*). Analysis of the alternating-access in protomers B and C is detailed in *SI Appendix*, *Supplementary Note 6* and Fig. S7. Detailed discussion on substrate dynamics and its interactions with the protein during OF⇌IF transition is also provided in *SI Appendix*, *Supplementary Note 7* and Fig. S8.

1.6. Lipid–Protein Interactions May Stabilize Distinct Conformational States. Despite the disparity between the protein dynamics, which is accelerated during the OF⇌IF transition simulations, and lipid dynamics, our simulations suggest that lipids may affect the structural transitions of Glt_{Ph}. In addition to the surface of Glt_{Ph}, which is largely membrane-exposed, lipids also directly interact with portions of TM7 and HP2, which are somewhat buried in the TD (*SI Appendix*, Fig. S9 *A–D*).

Other key regions, such as TM2, TM3, and TM5 also interact strongly with lipids and thus may be involved in lipid-dependent dynamics of the system. These regions show differential lipid

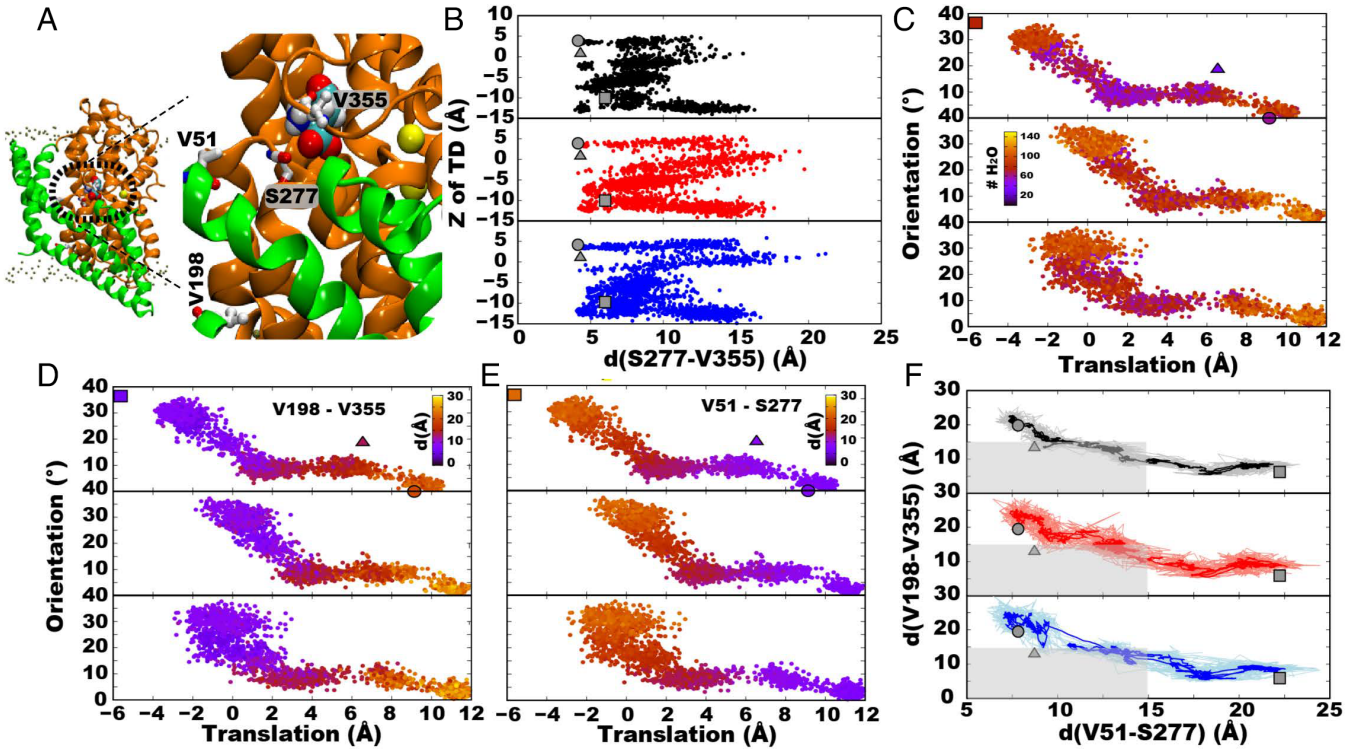

Fig. 6. Alternating access in the OF⇌IF transition of Glt_{Ph}. (*A*) Residues used in tracking the alternating access in the transporter. (*B*) Cα distance between S277 and V355 representing the HP tips during the transition. Black, red, and blue lines represent Glt_{fb}, Glt_{apo}, and Glt_{pb}, respectively. (*C*) Water accessibility of the HP tips as a function of TD translation and orientation. The water accessibility is defined as the number of water molecules within 5 Å of residues 275-280 (HP1) and 352-357 (HP2). (*D*) Distance between V198 and V355 representing the extracellular (EC) lock. (*E*) Distance between V51 and S277 representing the intracellular (IC) lock. (*F*) IC and EC lock distances plotted against each other show the working of the alternating access mechanism during the transition of the transporter. The gray area indicates the occluded region. *Top*, *Middle*, and *Bottom* plots represent Glt_{fb}, Glt_{apo}, and Glt_{pb}, respectively. Circle, square, and triangle indicators represent the values obtained from OF, IF, and iOF crystal structures, respectively.

interactions in the three simulated protomers and thereby lay the basis for any differences in conformational changes and energetics of each protomer (*SI Appendix*, Fig. S9 *A–D*).

Lipid tails insert into the space between protomers (interprotomeric lipids) as well as the interfacial space formed between SD and TD (interstitial lipids; *SI Appendix*, Fig. S9 *E* and *F*) within each protomer. The interstitial lipids are significant as they interact with residues forming the SD/TD interface and thus could directly affect the large-scale conformational transition in that protomer. The number of lipid heavy atoms interacting with the IF state is consistently higher than the OF state. Deep insertion of lipid tails at the interstitial spaces observed in our simulations is reminiscent of the lipid tail cocrystallized with the OF crystal structure [PDB ID. 2NWX (4)]. IF conformations did not show this level of deep lipid tail insertion. Based on the differential lipid insertion in the end states we may speculate that lipid interactions could preferentially stabilize a particular state. In fact, it has been previously suggested that the IF state strongly bends the lipid bilayer (34, 73). Such intimate lipid interactions may affect the energetics associated with the induced protein transition, in accord with the slight heterogeneity observed in the energy landscapes of the three protomers in our simulations (*SI Appendix*, Fig. S1), despite their threefold symmetry. We note that heterogeneous distribution of lipids around the three protomers is partly due to their slow diffusion constant around the proteins preventing them from complete sampling of the protomers at the same level. Interestingly, however, distinct binding of lipids to individual protomers is the most likely origin of their energy landscape heterogeneity. For the same reason, the accurate quantification of these interactions is quite challenging in that the lipid dynamics is quite slow and not particularly targeted for acceleration in our sampling protocol.

2. Concluding Remarks

This study provides a detailed model for the conformational transition of membrane-embedded Glt_{Ph} in three different binding states: i) with all three Na^+ ions and a substrate present in each protomer (Glt_{fb}), ii) with only one Na^+ present in each protomer (Glt_{pb}), and iii) in the *apo* state (Glt_{apo}). The transition from the OF⇌IF comprises a complex four-stage process, where the conformational change alternates between transnational and rotational movements of the TD with respect to the SD. Despite observing somewhat similar free-energy profiles for Glt_{fb} and Glt_{apo}, there exist distinct intermediates associated with the conformational transition mechanism, as previously suggested (19, 40). Notably, a single Na^+ ion bound at the Na_1^+ binding site in the absence of the substrate and other ions seem to lock the conformation of Glt_{Ph}, preventing any reasonable state transition. This aligns well with recent studies that the binding of two Na^+ ions to the Na_1^+ and Na_3^+ binding sites is imperative for complete HP2 gate opening, while the HP2 gate displays flexibility in the *apo* conformation (35, 74). The first stage of the transition involves disengagement of TD, which is likely induced by sliding of hydrophilic regions of HP1 over the hydrophobic SD, while in the later part of transition hydrophilic regions of HP2 slides against the SD, and interfacial area between TD and SD increases. The SD moves akin to a piston during the transition, showing an approximately 8 Å

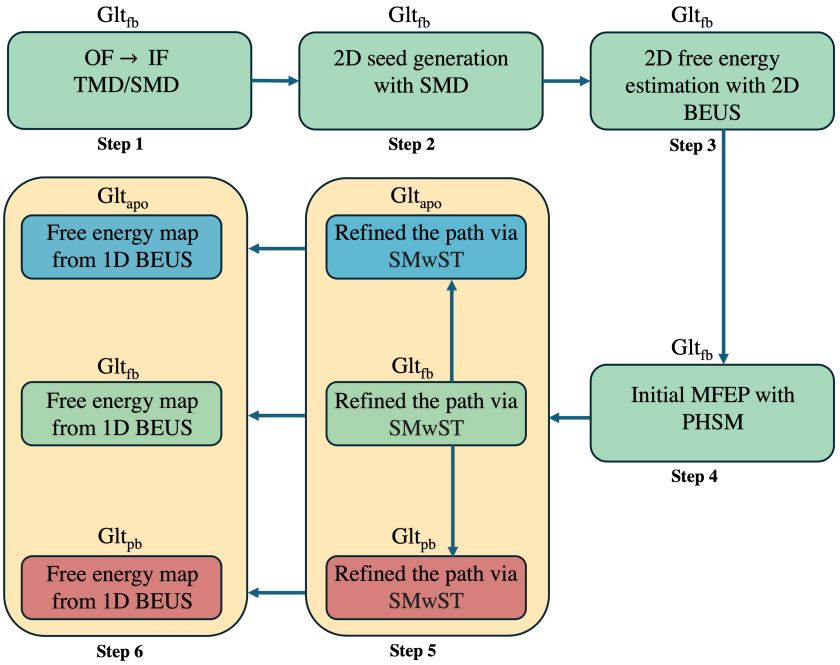

Fig. 7. Sampling protocol employed to investigate large-scale conformational changes during the OF⇌IF transition of Glt$_{Ph}$. Detailed system specifications and methodologies used in each step are given in *SI Appendix*, Table S1. The fully bound state (Glt$_{fb}$) is used until the step where the minimum free-energy path is derived. This path serves as the initial guess for the subsequent SMwST calculations (Step 5) in all states.

movement within the membrane. This movement corresponds with the elevator-like motions of TD, highlighting the critical role of SD–TD interactions in stabilizing the OF and IF states. Local conformational changes, such as the disruption of E192-K290 salt bridge between TM5 and HP1, TM7 helix alterations, and Na^+/substrate binding site dynamics, facilitate and contribute to the overall transition as well. Lipid–protein interactions, particularly in the buried regions of TD such as TM7 and HP2, may stabilize distinct conformational states, potentially contributing to the observed stability of the OF state. Structural intermediates obtained from the simulations include occluded conformations and transiently formed water-leaking states, which may be connected to the experimentally observed uncoupled Cl^- conductance (14). Biophysical and biochemical experiments may use the obtained structural information to design further experiments to trap the transporter in a specific conformation of interest. Other events in the transport cycle of Glt$_{Ph}$ such as binding and unbinding of substrate and Na^+ ions can be studied with the methodology used in this study. In addition, this approach and the CVs employed in this study can be generally applied to other transporters following the elevator-like mechanism.

3. Materials and Methods

Here, we present our computational methodology and outline our sampling protocols. Conventional MD simulations are often insufficient for investigating large-scale conformational changes in membrane transporters. Biased MD simulations, on the other hand, provide a more practical alternative to conventional MD for thermodynamic characterization of transporters. Various time-dependent or time-independent biasing potentials are used along with a post hoc or on the fly reweighting scheme to recover the unbiased statistics (61, 62). However, formulating such biasing protocols is challenging due to the high dimensionality and complexity of phase spaces in biomolecular systems. Identifying a CV space a priori that contains relevant conformations during the transition is a specific challenge as an erroneous choice of the CVs for biasing may lead to irrelevant transition pathways and misleading free-energy profiles. Additionally, inducing transitions using external forces may introduce artifacts, leading to nonphysical transition pathways. Our sampling strategy, particularly, aims to mitigate this issue.

Our workflow (Fig. 7) consists of six steps. We begin with a set of targeted MD (TMD) (75) as well as Steered MD (SMD) (76) simulations for the fully bound state (Glt$_{fb}$) to produce initial pathways for the OF⇌IF transition. Although these nonequilibrium simulations induce the OF⇌IF transition, the resulting pathways are not necessarily the most relevant and often nonphysical, involving a large amount of work. Therefore, we explore the entire 2D CV space using 2D BEUS (60–62) simulations to identify the most relevant pathway. SMD is then used as a seed generator for the subsequent 2D BEUS simulations, offering an estimate of the Glt$_{fb}$ 2D free-energy landscape in the selected CV space. Utilizing a post hoc string method (PHSM) (61, 62) with this map, we generate an initial minimum free-energy path (MFEP) for Glt$_{fb}$. While the PHSM path is a valuable starting point, it represents a reconstructed pathway that may not capture all relevant dynamical fluctuations and could deviate if subjected to free simulations. Therefore, this path undergoes refinement using a parallel version of the string method with swarms of trajectories (SMwST) (64). This iterative refinement ensures that the transition pathways are not only physically plausible but also relevant to the biological function of the transporter. The resulting path is then used as an initial guess also for SMwST simulations of the *apo* (Glt$_{apo}$) and partially bound (Glt$_{pb}$) states, as well. Finally, 1D BEUS simulations are conducted along the refined MFEPs to assess the energetics of the OF⇌IF transition for each system.

Our approach specifically relies on the BEUS method to continuously sample more degrees of freedom. However, refining reaction coordinates iteratively is crucial for accurate free-energy estimation in complex systems such as the one here. The string method helps identify the primary OF⇌IF transition pathway, creating a one-dimensional curve within a reduced subspace. Such a conformational transition pathway is relaxed and used not only to calculate the free energy associated with the transition but also to characterize both global and local protein conformational changes along the pathway. Technical details of the above steps, along with system preparation, MD simulations, and system-specific CVs are discussed in *SI Appendix, Methods*.

Data, Materials, and Software Availability. Representative structures corresponding to the minimum free energy regions in the OF, intermediate, and IF states, obtained from fully bound simulations, as well as movies related to SD/TD

interactions, are available at Zenodo. Additionally, input files (.psf, .pdb, .par) and configuration files (.conf) necessary to reproduce the results of this study are deposited at the same repository. All scripts, along with the full source code for PHSM, nonparametric reweighting, and a program for kernel construction from data, can also be accessed at Zenodo. Sample output files are provided as well. Simulation trajectories were generated using NAMD, while visualization and analysis were performed using VMD. Both software packages are publicly available (77).

ACKNOWLEDGMENTS. This research used resources of the Oak Ridge Leadership Computing Facility, which is a U. S. Department of Energy Office of Science User Facility supported under Contract DE-AC05-00OR22725 and the Blue Waters sustained-petascale computing project–which is supported by the NSF (award number ACI 1238993) and the state of Illinois. This research is supported by NIH grants U54-GM087519, R01-GM123455, P41-GM104601, R24-GM145965, R35-GM147423, and R15-GM139140 and NSF grant CHE 1945465.

Author affiliations: [a]Theoretical and Computational Biophysics Group, NIH Resource for Macromolecular Modeling and Visualization, Beckman Institute for Advanced Science and Technology, University of Illinois Urbana-Champaign, Urbana, IL 61801; [b]Department of Biochemistry, University of Illinois Urbana-Champaign, Urbana, IL 61801; [c]Center for Biophysics and Quantitative Biology, University of Illinois Urbana-Champaign, Urbana, IL 61801; [d]Department of Chemistry and Biochemistry, University of Arkansas, Fayetteville, AR 72701; and [e]Department of Chemistry, University of Illinois Urbana-Champaign, Urbana, IL 61801

1. Y. Kanai, M. A. Hediger, Primary structure and functional characterization of a high-affinity glutamate transporter. *Nature* **360**, 467–471 (1992).
2. G. Pines *et al*., Cloning and expression of a rat brain L-glutamate transporter. *Nature* **360**, 464–467 (1992).
3. W. A. Fairman, R. J. Vandenberg, J. L. Arriza, M. P. Kavanaugh, S. G. Amara, An excitatory amino-acid transporter with properties of a ligand-gated chloride channel. *Nature* **375**, 599–603 (1995).
4. O. Boudker, R. M. Ryan, D. Yernool, K. Shimamoto, E. Gouaux, Coupling substrate and ion binding to extracellular gate of a sodium-dependent aspartate transporter. *Nature* **445**, 387–393 (2007).
5. J. D. Rothstein, L. J. Martin, R. W. Kuncl, Decreased glutamate transport by the brain and spinal cord in amyotrophic lateral sclerosis. *N. Engl. J. Med.* **326**, 1464–1468 (1992).
6. S. Li, M. Mallory, M. Alford, S. Tanaka, E. Masliah, Glutamate transporter alterations in Alzheimer disease are possibly associated with abnormal APP expression. *J. Neuropathol. Exp. Neurol.* **56**, 901–911 (1997).
7. E. Masliah, M. Alford, R. DeTeresa, M. Mallory, L. Hansen, Deficient glutamate transport is associated with neurodegeneration in Alzheimer's disease. *Ann. Neurol.* **40**, 759–766 (1996).
8. K. Duerson *et al*., Detergent-insoluble EAAC1/EAAT3 aberrantly accumulates in hippocampal neurons of Alzheimer's disease patients. *Brain Pathol.* **19**, 267–278 (2009).
9. N. C. Danbolt, Glutamate uptake. *Prog. Neurobiol.* **65**, 1–105 (2001).
10. L. R. Forrest, R. Krämer, C. Ziegler, The structural basis of secondary active transport mechanisms. *Biochim. Biophys. Acta.* **1807**, 167–188 (2011).
11. R. J. Vandenberg, R. M. Ryan, Mechanisms of glutamate transport. *Physiol. Rev.* **93**, 1621–1657 (2013).
12. G. Verdon, S. Oh, R. N. Serio, O. Boudker, Coupled ion binding and structural transitions along the transport cycle of glutamate transporters. *eLife* **3**, e02283 (2014).
13. I. Hänelt, S. Jensen, D. Wunnicke, D. J. Slotboom, Low affinity and slow Na^+ binding precedes high affinity aspartate binding in the secondary-active transporter Glt_{Ph} *J. Biol. Chem.* **290**, 15962–15972 (2015).
14. J. C. Canul-Tec *et al*., Structure and allosteric inhibition of excitatory amino acid transporter 1. *Nature* **544**, 446–451 (2017).
15. J. L. Arriza, S. Eliasof, M. P. Kavanaugh, S. G. Amara, Excitatory amino acid transporter 5, a retinal glutamate transporter coupled to a chloride conductance. *Proc. Natl. Acad. Sci. U.S.A.* **94**, 4155–4160 (1997).
16. R. M. Ryan, A. D. Mitrovic, R. J. Vandenberg, The chloride permeation pathway of a glutamate transporter and its proximity to the glutamate translocation pathway. *J. Biol. Chem.* **279**, 20742–20751 (2004).
17. R. M. Ryan, J. A. Mindell, The uncoupled chloride conductance of a bacterial glutamate transporter homolog. *Nat. Struct. Mol. Biol.* **14**, 365–371 (2007).
18. I. Chen *et al*., Glutamate transporters have a chloride channel with two hydrophobic gates. *Nature* **591**, 327–331 (2021).
19. J. P. Machtens *et al*., Mechanisms of anion conduction by coupled glutamate transporters. *Cell* **160**, 542–553 (2015).
20. M. H. Cheng, D. Torres-Salazar, A. D. Gonzalez-Suarez, S. G. Amara, I. Bahar, Energy Landscape of the Substrate Translocation Equilibrium of Plasma-Membrane Glutamate Transporters. *eLife* **6**, e25850 (2017).
21. J. Wang, T. Albers, C. Grewer, Energy landscape of the substrate translocation equilibrium of plasma-membrane glutamate transporters. *J. Phys. Chem. B.* **122**, 28–39 (2018).
22. S. Pant, Q. Wu, R. Ryan, E. Tajkhorshid, Microscopic characterization of the chloride permeation pathway in the human Excitatory Amino Acid Transporter 1 (EAAT1). *ACS Chem. Neurosci.* **13**, 776–785 (2022).
23. N. Zerangue, M. P. Kavanaugh, Flux coupling in a neuronal glutamate transporter. *Nature* **383**, 634–637 (1996).
24. L. M. Levy, O. Warr, D. Attwell, Stoichiometry of the glial glutamate transporter GLT-1 expressed inducibly in a Chinese hamster ovary cell line selected for low endogenous Na^+-dependent glutamate uptake *J. Neurosci.* **18**, 9620–9628 (1998).
25. Y. Kanai *et al*., The neuronal and epithelial human high affinity glutamate transporter. Insights into structure and mechanism of transport. *J. Biol. Chem.* **269**, 20599–20606 (1994).
26. G. L. Ryan, A. D. Rutenberg, Clocking out: Modeling phage-induced lysis of *Escherichia coli*. *J. Bacteriol.* **189**, 4749–4755 (2007).
27. R. M. Ryan, E. L. Compton, J. A. Mindell, Functional characterization of a Na^+-dependent aspartate transporter from *Pyrococcus horikoshii J. Biol. Chem.* **284**, 17540–17548 (2009).
28. D. Yernool, O. Boudker, Y. Jin, E. Gouaux, Structure of a glutamate transporter homologue from *Pyrococcus horikoshii*. *Nature* **431**, 811–818 (2004).
29. N. Reyes, C. Ginter, O. Boudker, Transport mechanism of a bacterial homologue of glutamate transporters. *Nature* **462**, 880–885 (2009).
30. G. Verdon, O. Boudker, Crystal structure of an asymmetric trimer of a bacterial glutamate transporter homolog. *Nat. Struct. Mol. Biol.* **19**, 355–357 (2012).
31. N. Reyes, S. Oh, O. Boudker, Binding thermodynamics of a glutamate transporter homolog. *Nat. Struct. Mol. Biol.* **20**, 634–640 (2013).
32. N. Akyuz *et al*., Transport domain unlocking sets the uptake rate of an aspartate transporter. *Nature* **518**, 68–73 (2015).
33. S. Oh, O. Boudker, Kinetic mechanism of coupled binding in sodium-aspartate symporter Glt_{Ph}. *eLife* **7**, e37291 (2018).
34. X. Wang, O. Boudker, Large domain movements through the lipid bilayer mediate substrate release and inhibition of glutamate transporters. *eLife* **9**, e58417 (2020).
35. C. Alleva *et al*., Na^+-dependent gate dynamics and electrostatic attraction ensure substrate coupling in glutamate transporters. *Sci. Adv.* **6**, eaba9854 (2020).
36. G. H. M. Huysmans, D. Ciftci, X. Wang, S. C. Blanchard, O. Boudker, The high-energy transition state of the glutamate transporter homologue Glt_{Ph}. *EMBO J.* **40**, e105415 (2021).
37. K. D. Reddy, D. Ciftci, A. J. Scopelliti, O. Boudker, The archaeal glutamate transporter homologue Glt_{Ph} shows heterogeneous substrate binding. *J. Gen. Physiol.* **154**, e202213131 (2022).
38. M. Groeneveld, D. J. Slotboom, Rigidity of the subunit interfaces of the trimeric glutamate transporter GltT during translocation. *J. Mol. Biol.* **372**, 565–570 (2007).
39. I. Hänelt, D. Wunnicke, E. Bordignon, H. J. Steinhoff, D. J. Slotboom, Conformational heterogeneity of the aspartate transporter Glt(Ph). *Nat. Struct. Mol. Biol.* **20**, 210–214 (2013).
40. T. R. Matin, G. R. Heath, G. H. M. Huysmans, O. Boudker, S. Scheuring, Millisecond dynamics of an unlabeled amino acid transporter. *Nat. Commun.* **11**, 5016 (2020).
41. J. Jiang, I. H. Shrivastava, S. D. Watts, I. Bahar, S. G. Amara, Large collective motions regulate the functional properties of glutamate transporter trimers. *Proc. Natl. Acad. Sci. U.S.A.* **108**, 15141–15146 (2011).
42. S. Stolzenberg, G. Khelashvili, H. Weinstein, Structural intermediates in a model of the substrate translocation path of the bacterial glutamate transporter homologue Glt_{Ph}. *J. Phys. Chem. B* **116**, 5372–5383 (2012).
43. N. Akyuz, R. B. Altman, S. C. Blanchard, O. Boudkar, Transport dynamics in a glutamate transporter homologue. *Nature* **502**, 114–118 (2013).
44. G. B. Erkens, I. Nelt, J. M. Goudsmits, D. J. Slotboom, A. M. van Oijen, Unsynchronised subunit motion in single trimeric sodium-coupled aspartate transporters. *Nature* **502**, 119–123 (2013).
45. Y. Ruan *et al*., Direct visualization of glutamate transporter elevator mechanism by high-speed AFM. *Proc. Natl. Acad. Sci. U.S.A.* **114**, 1584–1588 (2017).
46. E. A. Riederer *et al*., A facile approach for the in vitro assembly of multimeric membrane transport proteins. *eLife* **7**, e36478 (2018).
47. V. Arkhipova, A. Guskov, D. J. Slotboom, Structural ensemble of a glutamate transporter homologue in lipid nanodisc environment. *Nat. Commun.* **11**, 998 (2020).
48. E. R. Georgieva, P. P. Borbat, C. Ginter, J. H. Freed, O. Boudker, Conformational ensemble of the sodium-coupled aspartate transporter. *Nat. Struct. Mol. Biol.* **20**, 215–221 (2013).
49. Z. Huang, E. Tajkhorshid, Identification of the third Na^+ site and the sequence of extracellular binding events in the glutamate transporter *Biophys. J.* **99**, 1416–1425 (2010).
50. Z. Tao, Z. Zhang, C. Grewer, Neutralization of the aspartic acid residue Asp-367, but not Asp-454, inhibits binding of Na^+ to the glutamate-free form and cycling of the glutamate transporter EAAC1 *J. Biol. Chem.* **281**, 10263–10272 (2006).
51. H. P. Larsson *et al*., Evidence for a third sodium-binding site in glutamate transporters suggests an ion/substrate coupling model. *Proc. Natl. Acad. Sci. U.S.A.* **107**, 13912–13917 (2010).
52. Z. Huang, E. Tajkhorshid, Dynamics of the extracellular gate and ion-substrate coupling in the glutamate transporter. *Biophys. J.* **95**, 2292–2300 (2008).
53. I. H. Shrivastava, J. Jiang, S. G. Amara, I. Bahar, Time-resolved mechanism of extracellular gate opening and substrate binding in a glutamate transporter. *J. Biol. Chem.* **283**, 28680–28690 (2008).
54. G. Grazioso *et al*., Investigating the mechanism of substrate uptake and release in the glutamate transporter homologue Glt_{Ph} through metadynamics simulations. *J. Am. Chem. Soc.* **134**, 453–463 (2012).
55. G. Heinzelmann, T. Bastug, S. Kuyucak, Mechanism and energetics of ligand release in the aspartate transporter Glt_{Ph}. *J. Phys. Chem. B* **117**, 5486–5496 (2013).
56. E. Zomot, I. Bahar, Intracellular gating in an inward-facing state of aspartate transporter Glt_{Ph} is regulated by the movements of the helical hairpin HP2. *J. Biol. Chem.* **288**, 8231–8237 (2013).
57. Y. Gu, I. H. Shrivastava, S. G. Amara, I. Bahar, Molecular simulations elucidate the substrate translocation pathway in a glutamate transporter. *Proc. Natl. Acad. Sci. U.S.A.* **106**, 2594–2598 (2009).
58. N. Silverstein, A. Sliman, T. Stockner, B. I. Kanner, Both reentrant loops of the sodium-coupled glutamate transporters contain molecular determinants of cation selectivity. *J. Biol. Chem.* **293**, 14200–14209 (2018).
59. J. Setiadi, S. Kuyucak, Free-energy simulations resolve the low-affinity Na^+-high-affinity asp binding paradox in Glt_{Ph} *Biophys. J.* **117**, 780–789 (2019).
60. Y. Sugita, A. Kitao, Y. Okamoto, Multidimensional replica-exchange method for free-energy calculations. *J. Chem. Phys.* **113**, 6042–6051 (2000).
61. M. Moradi, E. Tajkhorshid, Mechanistic picture for conformational transition of a membrane transporter at atomic resolution. *Proc. Natl. Acad. Sci. U.S.A.* **110**, 18916–18921 (2013).

62. M. Moradi, E. Tajkhorshid, Computational recipe for efficient description of large-scale conformational changes in biomolecular systems. *J. Chem. Theory Comput.* **10**, 2866–2880 (2014).
63. W. Ren, E. Vanden-Eijnden, P. Maragakis, E. Weinan, Transition pathways in complex systems: Application of the finite-temperature string method to the alanine dipeptide. *J. Chem. Phys.* **123**, 134109 (2005).
64. J. Pan, S. Tristram-Nagle, N. Kucerka, J. F. Nagle, Temperature dependence of structure, bending rigidity, and bilayer interactions of dioleoylphosphatidylcholine bilayers. *Biophys. J.* **94**, 117–124 (2008).
65. L. Maragliano, A. Fischer, E. Vanden-Eijnden, G. Ciccotti, String method in collective variables: Minimum free energy paths and isocommittor surfaces. *J. Chem. Phys.* **125**, 024106 (2006).
66. M. Chen, W. Yang, On-the-path random walk sampling for efficient optimization of minimum free-energy path. *J. Comput. Chem.* **30**, 1649–1653 (2009).
67. L. Cao, C. Lv, W. Yang, Hidden conformation events in DNA base extrusions: A generalized-ensemble path optimization and equilibrium simulation study. *J. Chem. Theory Comput.* **9**, 3756–3768 (2013).
68. N. Akyuz *et al*., Transport domain unlocking sets the uptake rate of an aspartate transporter. *Nature* **518**, 68–73 (2015).
69. O. Jardetzky, Simple allosteric model for membrane pumps. *Nature* **211**, 969–970 (1966).
70. J. Li *et al*., Transient formation of water-conducting states in membrane transporters. *Proc. Natl. Acad. Sci. U.S.A.* **110**, 7696–7701 (2013).
71. J. I. Wadiche, S. G. Amara, M. P. Kavanaugh, Ion fluxes associated with excitatory amino acid transport. *Neuron* **15**, 721–728 (1995).
72. R. M. Ryan, J. A. Mindell, The uncoupled chloride conductance of a bacterial glutamate transporter homolog. *Nat. Struct. Mol. Biol.* **14**, 365–371 (2007).
73. W. Zhou *et al*., Large-scale state-dependent membrane remodeling by a transporter protein. *eLife* **8**, e50576 (2019).
74. E. A. Riederer, P. Moënne-Loccoz, F. I. Valiyaveetil, Distinct roles of the Na^+ binding sites in the allosteric coupling mechanism of the glutamate transporter homolog, Glt_{Ph} *Proc. Natl. Acad. Sci. U.S.A.* **119**, e2121653119 (2022).
75. J. Schlitter, M. Engels, P. Krüger, Targeted molecular dynamics: A new approach for searching pathways of conformational transitions. *J. Mol. Graph.* **12**, 84–89 (1994).
76. S. Izrailev *et al*., "Steered molecular dynamics" in *Computational Molecular Dynamics: Challenges, Methods, Ideas*, P. Deuflhard *et al*., Eds. (Springer-Verlag, Berlin, Germany, 1998), pp. 39–65.
77. S. Thangapandian *et al*., Conformational free energy landscape of a glutamate transporter and microscopic details of its transport mechanism. Zenodo. https://doi.org/10.5281/zenodo.14885692. Deposited 19 February 2025.